Unusual anomalous Hall effect in perpendicularly magnetized YIG films with a small Gilbert damping constant

Q. B. Liu,[1,2] K. K. Meng,[1,*] Z. D. Xu,[3] Tao Zhu,[4] X. G. Xu,[1] J. Miao,[1] and Y. Jiang[1,†]

[1]*Beijing Advanced Innovation Center for Materials Genome Engineering, University of Science and Technology Beijing, Beijing 100083, China*

[2]*School of Applied and Engineering Physics, Cornell University, Ithaca, New York 14853, USA*

[3]*Department of Physics, South University of Science and Technology of China, Shenzhen 518055, China*

[4]*Institute of Physics, Chinese Academy of Sciences, Beijing 100190, China*

(Received 6 March 2020; revised manuscript received 19 April 2020; accepted 29 April 2020; published 20 May 2020)

The $Y_3Fe_5O_{12}$ (YIG) films with perpendicular magnetic anisotropy (PMA) have recently attracted a great deal of attention for spintronics applications. Here, we report the induced PMA in the YIG films grown on $(Gd_{2.6}Ca_{0.4})(Ga_{4.1}Mg_{0.25}Zr_{0.65})O_{12}$ (SGGG) substrates by epitaxial strain without preprocessing. Reciprocal space mapping shows that the films are lattice matched to the substrates without strain relaxation. Through ferromagnetic resonance and polarized neutron reflectometry measurements, we find that these YIG films have an ultralow Gilbert damping constant ($\alpha < 1 \times 10^{-5}$) and a magnetic dead layer, which is negligible at the YIG/SGGG interfaces. Moreover, the transport behavior of Pt/YIG/SGGG films reveals an enhancement of spin mixing conductance and a large unusual anomalous Hall effect (UAHE) as compared with $Pt/YIG/Gd_3Ga_5O_{12}$ (GGG) films. Although the UAHE in Pt/YIG/SGGG films show different characteristics with varying YIG thickness, they are all ascribed to the possible noncollinear magnetic order at the Pt/YIG interfaces induced by epitaxial strain.

DOI: 10.1103/PhysRevB.101.174431

I. INTRODUCTION

Spin transport in ferrimagnetic insulator (FMI) based devices has received considerable interest due to its free of current-induced Joule heating and beneficial for low-power spintronics applications [1,2]. Especially, the high-quality $Y_3Fe_5O_{12}$ (YIG) film as a widely studied FMI has low damping constant, low magnetostriction, and small magnetocrystalline anisotropy, making it a key material for magnonics and spin caloritronics. Though the magnons can carry information over distances as long as millimeters in YIG film, there remains a challenge to control its magnetic anisotropy while maintaining the low damping constant [3], especially for the thin film with perpendicular magnetic anisotropy (PMA), which is very useful for spin polarizers, spin-torque oscillators, magneto-optical devices, and magnon valves [4–7]. In addition, the spin-orbit torques (SOTs) induced magnetization switching with low current densities has been realized in nonmagnetic heavy metal (HM)/FMI heterostructures, paving the road towards ultralow-dissipation SOT devices based on FMIs [8–10]. Furthermore, previous theoretical studies have pointed that the current density will become much smaller if the domain structures were topologically protected (chiral) [11]. However, most FMI films favor an in-plane magnetic easy axis dominated by shape anisotropy, and the investigation is eclipsed as compared with ferromagnetic materials, which show abundant and interesting domain structures such as chiral domain walls and magnetic skyrmions, *et al.* [12–17]. Recently, the interface-induced chiral domain walls have been observed in centrosymmetric oxides $Tm_3Fe_5O_{12}$ (TmIG) thin films, and the domain walls can be propelled by the spin current from an adjacent platinum layer [18]. Similar to the TmIG films, the possible chiral magnetic structures are also expected in the YIG films with lower damping constant, which would further improve the chiral domain walls' motion speed [19].

Recently, several ways have been reported to attain perpendicularly magnetized YIG films, one of which is utilizing the lattice distortion and magnetoelastic effect induced by epitaxial strain [20–23]. It is noted that strain control cannot only enable field-free magnetization switching but also assist stabilization of the noncollinear magnetic textures in a broad range of magnetic field and temperature. Therefore, abundant and interesting physical phenomena could emerge in epitaxial grown YIG films with PMA. However, either varying buffer layer or doping could increase the Gilbert damping constant of YIG, which will affect the efficiency of SOT-induced magnetization switching [21,22]. On the other hand, this preprocessing would lead to more complicated magnetic structures and impede further discussion of spin transport properties such as the possible topological Hall effect (THE).

In this work, we realized the PMA YIG films deposited on $(Gd_{2.6}Ca_{0.4})(Ga_{4.1}Mg_{0.25}Zr_{0.65})O_{12}$ (SGGG) substrates due to epitaxial strain. Through ferromagnetic resonance (FMR) and polarized neutron reflectometry (PNR) measurements,

*kkmeng@ustb.edu.cn
†yjiang@ustb.edu.cn

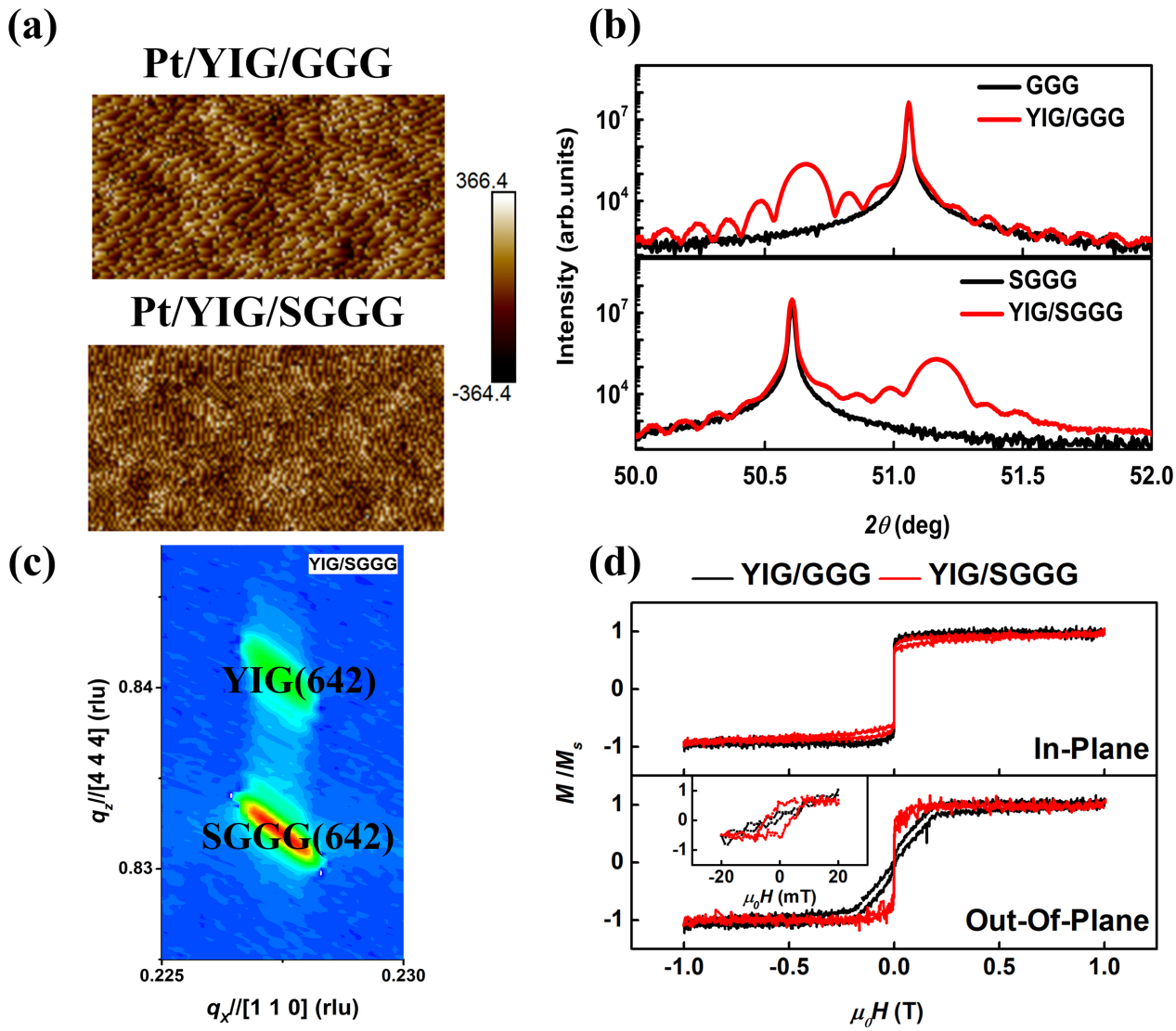

FIG. 1. (a) AFM images of the YIG films grown on two substrates (scale bar, 1 μm). (b) XRD ω-2θ scans of the two different YIG films grown on two substrates. (c) High-resolution XRD reciprocal space map of the 40-nm-thick YIG film grown on SGGG substrate. (d) Field dependence of the normalized magnetization of the 40-nm-thick YIG films grown on two different substrates.

we have found that the YIG films had small Gilbert damping constant and magnetic dead layer is negligible at the YIG/SGGG interfaces. Moreover, we have carried out the YIG thickness dependence of transport measurements in Pt/YIG/SGGG films and observed large unusual anomalous Hall effect (UAHE), which did not exist in the compared Pt/YIG/GGG films. The UAHE in both Pt/YIG(3 nm)/SGGG and Pt/YIG(40 nm)/SGGG films are all ascribed to the possible noncollinear magnetic order at the Pt/YIG interfaces induced by epitaxial strain.

II. METHODS

The epitaxial YIG films with varying thickness from 3 to 90 nm were grown on [111]-oriented GGG substrates (lattice parameter $a = 1.237$ nm) and SGGG substrates (lattice parameter $a = 1.248$ nm), respectively by pulsed laser deposition technique. The growth temperature was $T_S = 780\,^{\circ}$C and the oxygen pressure was varied from 10 to 50 Pa. Then, the films were annealed at 780 °C for 30 min at the oxygen pressure of 200 Pa. The Pt (5 nm) layer was deposited on top of YIG films at room temperature by magnetron sputtering. After position, electron beam lithography and Ar ion milling were used to pattern Hall bars, and a lift-off process was used to form contact electrodes. The size of all the Hall bars is 20 μm × 120 μm. After the deposition, we have investigated the surface morphology of the two kinds of films using atomic force microscopy (AFM) as shown in Fig. 1(a), and the two films have similar and small surface roughness ∼0.1 nm. Figure 1(b) shows enlarged x-ray diffraction (XRD) ω-2θ scan spectra of 40-nm-thick YIG films grown on two different substrates, and more details are shown in the Supplemental Material Note 1 [24], and they all show predominant (444) diffraction peaks without any other diffraction peaks, excluding impurity phases or other crystallographic orientations and indicating single-phase nature. According to the (444) diffraction peak position and the reciprocal space map (RSM) of (642) reflection of a 40-nm-thick YIG film grown on

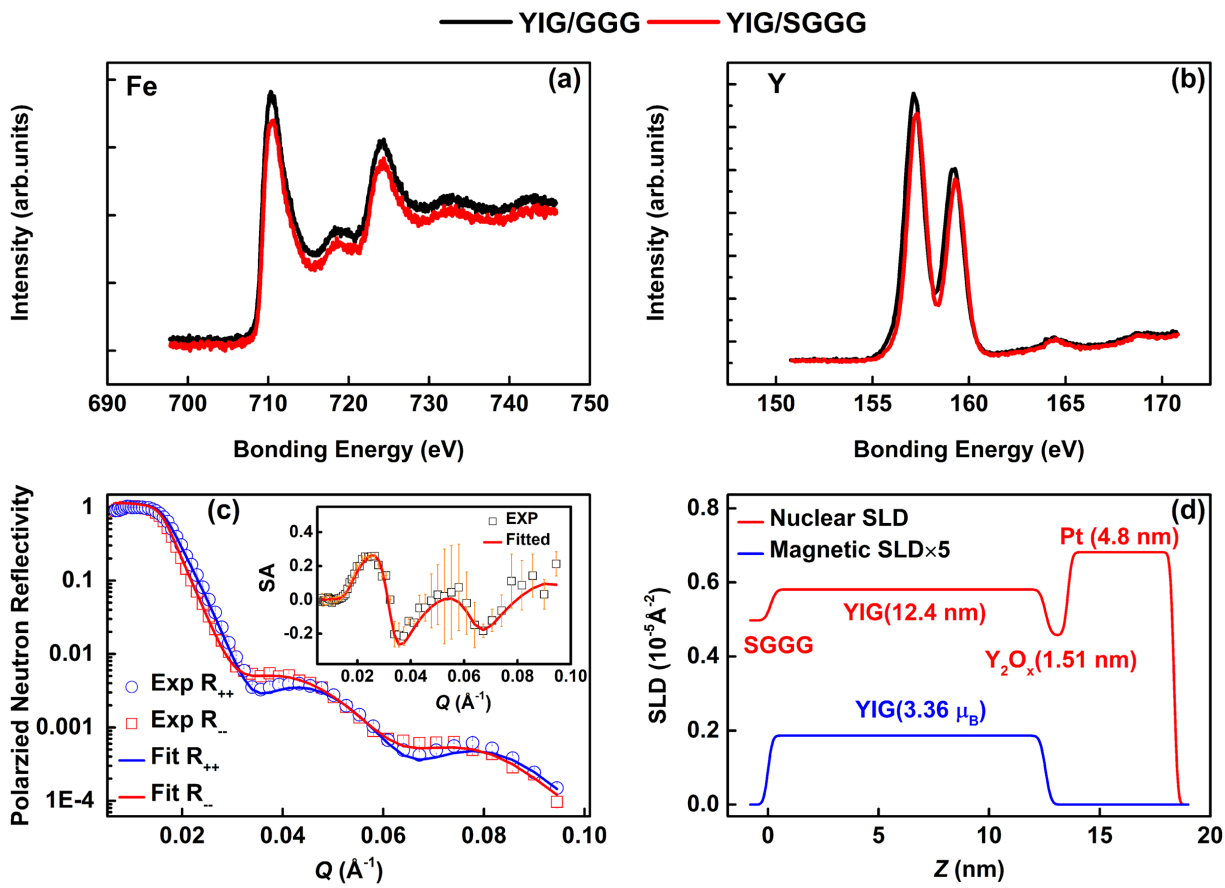

FIG. 2. Room temperature XPS spectra of (a) Fe *2p* and (b) Y *3d* for YIG films grown on two substrates. (c) PNR signals (with a 900-mT in-plane field) for the spin-polarized R_{++} and R_{--} channels. Inset: The experimental and simulated SA as a function of scattering vector Q. (d) SLD profiles of the YIG/SGGG films. The nuclear SLD and magnetic SLD is directly proportional to the nuclear scattering potential and the magnetization, respectively.

SGGG as shown in Fig. 1(c), we have found that the lattice constant of SGGG (∼1.248 nm) substrate was larger than YIG layer (∼1.236 nm). We quantify this biaxial strain as $\xi = (a_{OP} - a_{IP})/a_{IP}$, where a_{OP} and a_{IP} represent pseudo cubic lattice constant calculated from out-of-plane lattice constant $d(4\,4\,4)_{OP}$ and in-plane lattice constant $d(1\,1\,0)_{IP}$, respectively, following the equation of $d = \frac{a}{\sqrt{h^2+k^2+l^2}}$, with h, k, and l standing for Miller indices of the crystal planes. It indicates that the SGGG substrate provides tensile stress ($\xi \sim 0.84\%$) [22]. At the same time, the magnetic properties of the YIG films grown on two different substrates were measured via vibrating sample magnetometry at room temperature. According to the magnetic field ($\mu_0 \boldsymbol{H}$) dependence of magnetization ($\boldsymbol{M}$) as shown in Fig. 1(d) and Fig. S2 [24], the magnetic anisotropy of YIG films grown on SGGG substrates have been modulated by strain, while they show similar in-plane behaviors with normal YIG/GGG films.

III. RESULTS AND DISCUSSION

To further investigate the quality of YIG films grown on SGGG substrates and exclude the possibility of the strain induced large stoichiometry and lattice mismatch, compositional analyses were carried out using x-ray photoelectron spectroscopy (XPS) and PNR. As shown in Fig. 2(a), the difference of binding energy between the $2p_{3/2}$ peak and the satellite peak is about 8.0 eV, and the Fe ions are determined to be in the 3^+ valence state. It is found that there is no obvious difference for Fe elements in YIG films grown on GGG and SGGG substrates. The Y *3d* spectrums show small energy shift as shown in Fig. 2(b) and the binding energy shift may be related to lattice strain and variation of bond length [22]. Therefore, the stoichiometry of YIG surface has not been dramatically modified with strain control. Furthermore, we have performed PNR measurement to probe depth dependent structure and magnetic information of YIG films grown on SGGG substrates. The PNR signals and scattering length density (SLD) profiles for YIG (12.8 nm)/SGGG films by applying an in-plane magnetic field of 900 mT at room temperature are shown in Figs. 2(c) and 2(d), respectively. In Fig. 2(c), R_{++} and R_{--} are the non-spin-flip reflectivities, where the spin polarizations are the same for the incoming and reflected neutrons. The inset of Fig. 2(c) shows the experimental and simulated spin asymmetry (SA), defined as $\mathrm{SA} = (R_{++} - R_{--})/(R_{++} + R_{--})$, as a function of scattering vector Q. A reasonable fit was obtained with a three-layer model for the single YIG film, containing the interface layer, main YIG layer, and surface layer. The nuclear SLD and magnetic SLD are directly proportional to the nuclear scattering potential and the magnetization, respectively. Then, the depth-resolved

structural and magnetic SLD profiles delivered by the fitting are shown in Fig. 2(d). The $\boldsymbol{Z}$ axis represents the distance for the vertical direction of the film, where $\boldsymbol{Z} = 0$ indicates the position at the YIG/SGGG interfaces. It is obvious that there is little Gd diffusion into the YIG film, and the dead layer is much thinner than the reported values (5–10 nm) between YIG (or TmIG) and substrates [33–35]. The net magnetization of YIG is 3.36 μ_B (∼140 KA/m), which is similar to that of bulk YIG [36]. The PNR results also showed that besides the YIG/SGGG interfaces region, there is also 1.51-nm-thick nonmagnetic surface layer, which may be Y_2O_3 and is likely to be extremely important in the magnetic proximity effect [33].

To quantitatively determine the magnetic anisotropy and dynamic properties of YIG films, the FMR spectra were measured at room temperature using an electron paramagnetic resonance spectrometer with rotating the films. Figure 3(a) shows the geometric configuration of angle-resolved FMR measurements. For FMR measurements, the DC magnetic field was modulated with AC field. The transmitted signal was detected by a lock-in amplifier. We carried out the FMR spectrum by sweeping external magnetic field. The data obtained were then fitted to a sum of symmetric and antisymmetric Lorentzian function to extract the linewidth. We use the FMR absorption line shape to extract resonance field ($\mu_0 H_{\rm res}$) and peak-to-peak linewidth ($\mu_0 \Delta H_{\rm pp}$) at different θ for 40-nm-thick YIG films grown on GGG and SGGG substrates, respectively. The results for 3-nm-thick YIG films are shown in the Supplemental Material Note 3 [24]. According to the angle dependence of $\mu_0 H_{\rm res}$ as shown in Fig. 3(b), one can find that as compared with YIG films grown on GGG substrates, the minimum $\mu_0 H_{\rm res}$ of 40-nm-thick YIG film grown on SGGG substrate increases with varying θ from 0° to 90°. We have also quantified through the FMR results the anisotropy field $\mu_0 H_k^{\rm eff}$ and the effective magnetization $\mu_0 M_{\rm eff} = \mu_0 M_s - \mu_0 H_k^{\rm eff}$ of YIG (40 nm)/SGGG films, and the values are 23.82 and 149.58 mT, respectively. More detailed information about the procedure is shown in the Supplemental Material Note 3 [24]. On the other hand, according to the frequency dependence of $\mu_0 H_{\rm res}$ for 40-nm-thick YIG films with applying $\mu_0 \boldsymbol{H}$ in the XY plane as shown in Fig. 3(c), in contrast to YIG/GGG films, the $\mu_0 H_{\rm res}$ in YIG/SGGG films could not be fitted by the in-plane magnetic anisotropy Kittel formula $f = (\gamma/2\pi)[\mu_0 H_{\rm res}(\mu_0 H_{\rm res} + 4\pi M_{\rm eff})]^{1/2}$ and more detailed discussion is shown in Supplemental Material Note 3 [24]. All the results indicate that the easy axis of YIG (40 nm)/SGGG films lies out-of-plane. The angle dependent $\mu_0 \Delta H_{\rm pp}$ are also compared as shown in Fig. 3(d), the 40-nm-thick YIG film grown on SGGG substrate has an optimal value of $\mu_0 \Delta H_{\rm pp}$ as low as 0.4 mT at $\theta = 64°$, and the corresponding FMR absorption line and Lorentz fitting curve are shown in Fig. 3(e). Generally, the $\mu_0 \Delta H_{\rm pp}$ is expected to be minimum (maximum) along the magnetic easy (hard) axis, which is basically coincident with angle dependent $\mu_0 \Delta H_{\rm pp}$ for the YIG film grown on GGG substrates. However, as shown in Fig. 3(d), the $\mu_0 \Delta H_{\rm pp}$ for YIG/SGGG films shows an anomalous variation. The lowest $\mu_0 \Delta H_{\rm pp}$ at $\theta = 64°$ could be ascribed to high YIG film quality and ultrathin magnetic dead layer at the YIG/SGGG interfaces. It should be noted that, as compared with YIG/GGG films, the $\mu_0 \Delta H_{\rm pp}$ is independent on the frequency from 5 to 14 GHz as shown in Fig. 3(f). Then, we have calculated the Gilbert damping constant α of YIG (40 nm)/SGGG films by extracting $\mu_0 \Delta H_{\rm pp}$ at each frequency as shown in Fig. 3(f). The obtained α is smaller than 1×10^{-5}, which is one order of magnitude lower than the results in Ref. [21] and would open perspectives for magnetization dynamics. According to the theoretical theme, the $\mu_0 \Delta H_{\rm pp}$ consists of three parts: Gilbert damping, two magnons scattering relaxation process and inhomogeneities, in which both Gilbert damping and two-magnons-scattering relaxation process depend on frequency. Therefore, the large $\mu_0 \Delta H_{\rm pp}$ in YIG/SGGG films mainly stems from inhomogeneities, which will be discussed next with the help of transport measurements.

Notably, although the 3-nm-thick YIG film grown on SGGG has not shown PMA as compared with YIG (40 nm)/SGGG films, the FMR results of YIG (3 nm)/SGGG films reveal different magnetic anisotropy with YIG (3 nm)/GGG films as discussed in Supplemental Material Note 3 [24], indicating the strain will also modify the magnetic anisotropy of thinner YIG films. To further explore the strain-induced magnetic order, we have investigated the YIG thickness dependence of spin transport properties in Pt/YIG SGGG films, which are basically sensitive to magnetic details of YIG films. The magnetoresistance (MR) has been proved as a powerful tool to effectively explore magnetic information originating from the interfaces [37]. The temperature dependent spin Hall magnetoresistance (SMR) of Pt (5 nm)/YIG (3 nm) films grown on two different substrates were measured using a small and nonperturbative current density ($\sim 1 \times 10^6$ A/cm^2), and the sketches of the measurement are shown in Fig. 4(a). It should be noted that the influence of thermoelectric/thermomagnetic effect can be negligible in our samples as discussed in Supplemental Material Note 4 [24]. The β scan of longitudinal MR, which is defined as $\mathrm{MR} = \Delta\rho_{XX}/\rho_{XX}(0) = [\rho_{XX(b)} - \rho_{XX(0)}]/\rho_{XX(0)}$ in the YZ plane for the two films under a 3 T field (enough to saturate the magnetization of YIG), shows $\cos^2\beta$ behaviors with varying temperature for Pt/YIG/GGG and Pt/YIG/SGGG films as shown in Figs. 4(b) and 4(c), respectively. The SMR of Pt/YIG/SGGG films is larger than that of Pt/YIG/GGG films with the same thickness of YIG at room temperature, indicating an enhancement of spin mixing conductance ($G_{\uparrow\downarrow}$) in the Pt/YIG/SGGG films. Here, the spin transport properties of Pt layers are expected to be the same because of the similar resistivity and films quality. Therefore, the SGGG substrate not only induces PMA but also enhances $G_{\uparrow\downarrow}$ at the Pt/YIG interfaces. We have also investigated the field dependent Hall resistivities in Pt/YIG (3 nm)/SGGG films in the temperature range from 260 to 350 K as shown in Fig. 4(d). Though the conduction electrons cannot penetrate into the FMI layer, the possible anomalous Hall effect (AHE) at the HM/FMI interfaces is proposed to emerge, and the total Hall resistivity can usually be expressed as the sum of various contributions [38,39]:

$$\rho_H = R_0 \mu_0 H + \rho_S + \rho_{S\text{-}A}, \tag{1}$$

where R_0 is the normal Hall coefficient, ρ_S is the transverse manifestation of SMR, and $\rho_{S\text{-}A}$ is the spin Hall anomalous Hall effect (SHAHE) resistivity. Notably, the external field is applied out-of-plane, and $\rho_s(\sim \Delta\rho_1 m_x m_y)$ can be neglected

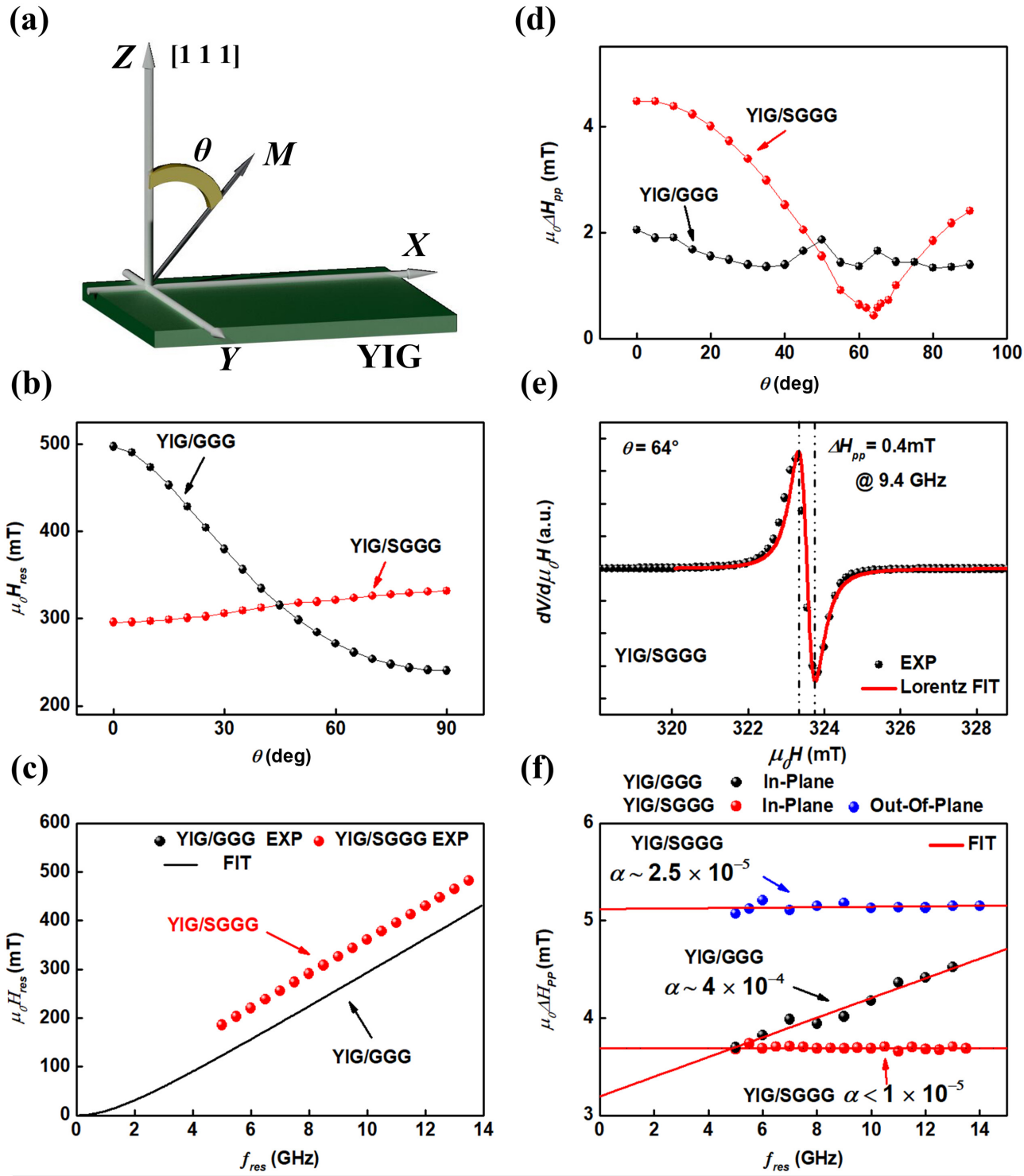

FIG. 3. (a) The geometric configuration of the angle dependent FMR measurement. (b) The angle dependence of the $\mu_0 H_{\rm res}$ for the 40-nm-thick YIG films grown on GGG and SGGG substrates. (c) The frequency dependence of the $\mu_0 H_{\rm res}$ for 40-nm-thick YIG films grown on GGG and SGGG substrates. (d) The angle dependence of $\mu_0 \Delta H_{\rm pp}$ for the 40-nm-thick YIG films grown on GGG and SGGG substrates. (e) FMR spectrum of the 40-nm-thick YIG film grown on SGGG substrate with 9.46 GHz at $\theta = 64^\circ$. (f) The frequency dependence of $\mu_0 \Delta H_{\rm pp}$ for the 40-nm-thick YIG films grown on GGG and SGGG substrates.

[32]. Interestingly, as compared with the total Hall resistivities of Pt/YIG(3 nm)/GGG films as discussed in Supplemental Material Note 5 [24], the YIG films grown on SGGG substrate show bump and dip features during the hysteretic measurements in the temperature range from 260 to 350 K. In the following discussion, we term the part of extra Hall signals as $\rho_{U\text{-}S\text{-}A}$. The $(\rho_{S\text{-}A} + \rho_{U\text{-}S\text{-}A})$ clearly coexist with the large background of a normal Hall effect. Notably, the broken (space) inversion symmetry with strong spin-orbit coupling will induce the Dzyaloshinskii-Moriya interaction (DMI). If

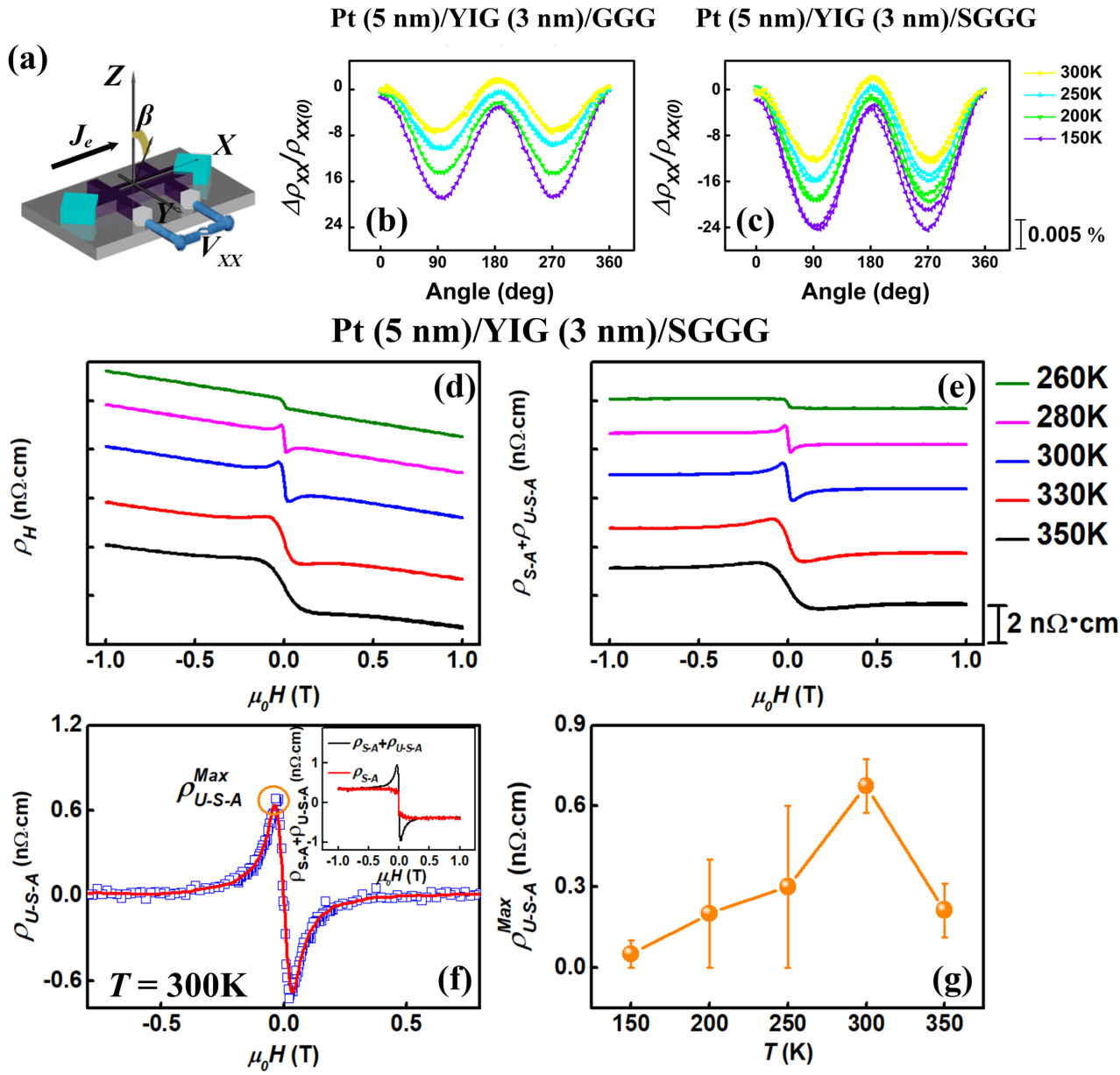

FIG. 4. (a) The definition of the angle, the axes and the measurement configurations. (b) and (c) Longitudinal MR at different temperatures in Pt/YIG/GGG and Pt/YIG/SGGG films, respectively (The applied magnetic field is 3 T). (d) Total Hall resistivities $vs\mu_0\boldsymbol{H}$ for Pt/YIG(3 nm)/SGGG films in the temperature range from 260 to 300 K. (e) $(\rho_{S\text{-}A}+\rho_{U\text{-}S\text{-}A})$ $vs\mu_0\boldsymbol{H}$ for two films in the temperature range from 260 to 300 K. (f) $\rho_{U\text{-}S\text{-}A}vs\mu_0\boldsymbol{H}$ for Pt/YIG(3 nm)/SGGG films at 300K. Inset: $\rho_{S\text{-}A}$ and $\rho_{S\text{-}A}+\rho_{U\text{-}S\text{-}A}vs\mu_0\boldsymbol{H}$ for Pt/YIG(3 nm)/SGGG films at 300K. (g) Temperature dependence of the $\rho^{\mathrm{Max}}_{U\text{-}S\text{-}A}$. We have carried out the transport properties of many samples for several times, and the data have been label−ed with error bars.

the DMI could be compared with the Heisenberg exchange interaction and the magnetic anisotropy that were controlled by strain, it could stabilize noncollinear magnetic textures such as skyrmions, producing a fictitious magnetic field and THE. The $\rho_{U\text{-}S\text{-}A}$ indicates that a chiral spin texture may exist, which is similar to B20-type compounds MnSi and MnGe [40,41]. To more clearly demonstrate the origin of $\rho_{U\text{-}S\text{-}A}$, we have extracted it by subtracting the normal Hall term as discussed in Supplemental Material Note 6 [24], and the temperature dependence of $(\rho_{S\text{-}A}+\rho_{U\text{-}S\text{-}A})$ has been shown in Fig. 4(e). Then, we can further discern the peak and hump structures in the temperature range from 260 to 350 K. The SHAHE contribution $\rho_{S\text{-}A}$ can be expressed as $\rho_{S\text{-}A}=-\Delta\rho_2 m_Z$ [38,42,43], where $\Delta\rho_2$ is the coefficient depending on the imaginary part of $G_{\uparrow\downarrow}$, and m_z is the magnetization along $\boldsymbol{Z}$ direction. The further extracted $\rho_{U\text{-}S\text{-}A}$ has been shown in Fig. 4(f), and the temperature dependence of the largest $\rho_{U\text{-}S\text{-}A}$ $(\rho^{\mathrm{Max}}_{U\text{-}S\text{-}A})$ in all the films have been shown in Fig. 4(g). Finite values of $\rho^{\mathrm{Max}}_{U\text{-}S\text{-}A}$ exist in the temperature range from 150 to 350 K, which is much different from that in B20-type bulk chiral magnets, which are subjected to low temperature and large magnetic field [44]. The large nonmonotonic magnetic

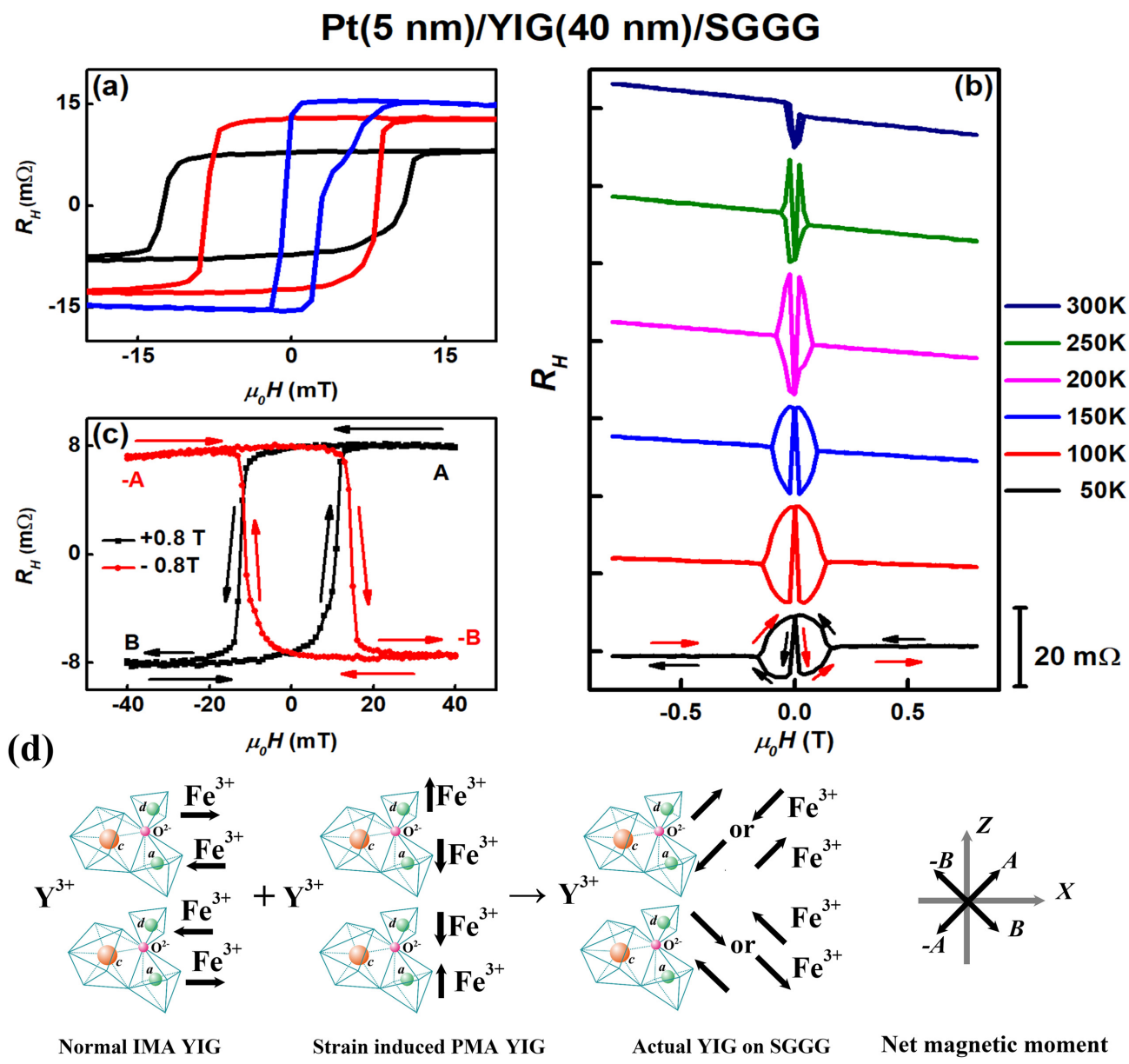

FIG. 5. (a) and (b) The Hall resistances *vs*$\mu_0 \boldsymbol{H}$ for the Pt/YIG(40 nm)/SGGG films in the temperature range from 50 to 150 K in small and large magnetic field range, respectively. (c) The Hall resistances *vs* $\mu_0 \boldsymbol{H}$ at small magnetic field range after sweeping a large out-of-plane magnetic field +0.8 T (black line) and −0.8 T (red line) to zero. (d) An illustration of the orientations of the magnetizations Fe (*a*) and Fe (*d*) in YIG films with the normal in-plane magnetic anisotropy (IMA), the ideal strain induced PMA and the actual magnetic anisotropy grown on SGGG substrates in our work.

field dependence of anomalous Hall resistivity could not stem from the Weyl points, and a more detailed discussion is found in Supplemental Material Note 7 [24].

Furthermore, robust UAHE with different characteristics as compared with Pt (5 nm)/YIG (3 nm)/SGGG films has also been found in Pt (5 nm)/YIG (40 nm)/SGGG films. First, we have investigated the small field dependence of the Hall resistances for Pt (5 nm)/YIG (40 nm)/SGGG films as shown in Fig. 5(a), and more details are shown in Supplemental Material Note 8 [24]. The out-of-plane hysteresis loops of Pt/YIG/SGGG films are not central symmetry, indicating the existence of an internal field leading to opposite velocities of up to down and down to up domain walls in the presence of current along the $+\boldsymbol{X}$ direction. The large field dependences of the Hall resistances are shown in Fig. 5(b), which could not be described by Eq. (1). There are large variations for the Hall signals when external magnetic field is lower than saturation field ($\mu_0 M_s$) of YIG films (∼50 mT at 300 K and ∼150 mT at 50 K). More interestingly, we have applied a large out-of-plane external magnetic field of +0.8 T (−0.8 T) above $\mu_0 M_s$ to saturate the out-of-plane magnetization component $\boldsymbol{M_Z} > 0 (\boldsymbol{M_Z} < 0)$, then decreased the field to zero, finally the Hall resistances were measured in the small field range (± 40 mT), from which we could find that the shape was reversed as shown in Fig. 5(c). Here, we infer that the magnetic structures at the Pt/YIG interfaces could not be a simple linear magnetic order. Theoretically, an additional chirality-driven Hall effect might be present in the ferromagnetic

regime due to spin canting [45–48]. It has been found that the strain from an insulating substrate could produce tetragonal distortion, which would drive orbital selection, modifying electronic properties and magnetic ordering of manganites. For $A_{1-x}B_xMnO_3$ perovskites, a compressive strain makes the ferromagnetic configuration relatively more stable than the antiferromagnetic state [49]. On the other hand, the strain could induce spin canting [50]. A variety of experiments and theories have reported that ion substitute, defect, and magnetoelastic interaction would cant the magnetization of YIG [51–53]. Therefore, if we could modify the magnetic order by epitaxial strain, the noncollinear magnetic structure is expected to emerge in YIG films. For YIG crystalline structure, the two Fe sites are located on octahedrally coordinated 16(a) site and tetrahedrally coordinated 24(d) site, aligning antiparallel with each other [28]. According to the XRD and RSM results, the tensile strain due to SGGG substrate would result in a distortion angle of the facets of the YIG unit cell smaller than 90° [54]. Therefore, the magnetization of Fe atoms at two sublattices should be discussed separately rather than as a whole. Then, the unusual signals of Pt/YIG/SGGG films could be ascribed to the emergence of four different Fe^{3+} magnetic orientations in strained Pt/YIG films as shown in Fig. 5(d). To be more clearly, we assume that, in analogy with ρ_S, the $\rho_{U\text{-}S\text{-}A}$ is larger than $\rho_{S\text{-}A}$ and scales linearly with $m_y m_z$ and $m_x m_z$. With applying a large external field $\mu_0\boldsymbol{H}$ along the $\boldsymbol{Z}$ axis, the uncompensated magnetic moment at tetrahedrally coordinated 24(d) is along with external fields $\mu_0\boldsymbol{H}$ direction for $|\mu_0\boldsymbol{H}| > \mu_0 M_{\mathbf{s}}$, and the magnetic moment tends to be along $\boldsymbol{A}(-\boldsymbol{A})$ axis when external field is swept from 0.8 T (−0.8 T) to 0 T. Then, if the Hall resistance was measured at a small out-of-plane field, the uncompensated magnetic moment would switch from the $\boldsymbol{A}(-\boldsymbol{A})$ axis to the $\boldsymbol{B}(-\boldsymbol{B})$ axis. In this case, the $\rho_{U\text{-}S\text{-}A}$ that scales with $\Delta\rho_3(m_y m_z + m_x m_z)$ would change sign because $m_{\mathbf{z}}$ is switched from the $\boldsymbol{Z}$ axis to the $-\boldsymbol{Z}$ axis as shown in Fig. 5(c). However, there is still some problem that needs to be further clarified. There are no unusual signals in Pt/YIG/GGG films that could be ascribed to the weak strength of $\Delta\rho_3$ or strong magnetic anisotropy. It is still valued for further discussion of the origin of $\Delta\rho_3$ whether it could stem from skrymions *et al.*, but until now we have not observed any chiral domain structures in Pt/YIG/SGGG films through Lorentz transmission electron microscopy. Finally, we want to mention that, as shown in Figs. 4(d) and 5(b), the Hall measurements in Pt/YIG (3 nm)/SGGG and Pt/YIG (40 nm)/SGGG films are different, which could be related to the thickness dependence of magnetic anisotropy in YIG/SGGG films. Notably, according to the FMR results, although the magnetic anisotropy is different in YIG (3 nm)/SGGG and YIG (40 nm)/SGGG films, a similar magnetic order will exist for both films and we should discriminate it from the normal YIG/GGG films. The mechanisms that determine the UAHE are very complex, but the dominant role could be the modified magnetic order induced by strain. We hope that future work would involve more detailed magnetic microscopy imaging and microstructure analysis, which can further elucidate the real microscopic origin of large nonmonotonic magnetic field dependence of anomalous Hall resistivity.

IV. CONCLUSION

In conclusion, PMA YIG films could be realized using epitaxial strain. These YIG films grown on SGGG substrates had low Gilbert damping constants ($<1\times10^{-5}$) and the magnetic dead layer is negligible at the YIG/SGGG interfaces. Moreover, we observed large UAHE in Pt/YIG/SGGG films with varying YIG thickness, which did not exist in the compared Pt/YIG/GGG films. The UAHE in Pt/YIG/SGGG films are all ascribed to the possible noncollinear magnetic order at the Pt/YIG interfaces induced by epitaxial strain. The present work not only demonstrates that the strain control can effectively tune the electromagnetic properties of FMI but also open up the exploration of noncollinear spin texture for fundamental physics and magnetic storage technologies based on FMI.

ACKNOWLEDGMENTS

The authors thank Prof. L. Q. Yan and Prof. Y. Sun for the technical assistance in ferromagnetic resonance measurement. This work was partially supported by the National Science Foundation of China (Grants No. 51971027, No. 51971024, No. 51927802, No. 51971023, No. 51971027, and No. 51731003), and the Fundamental Research Funds for the Central Universities (FRF-TP-19-001A3).

[1] A. Hoffmann and M. Wu, *Recent Advances in Magnetic Insulators-from Spintronics to Microwave Applications* (Academic, Burlington, 2013).
[2] S. Maekawa, *Concepts in Spin Electronics* (Oxford University Press, Oxford, 2006).
[3] S. Neusser and D. Grundler, Adv. Mater. **21**, 2927 (2009).
[4] Y. Kajiwara, K. Harii, S. Takahashi, J. Ohe, K. Uchida, M. Mizuguchi, H. Umezawa, H. Kawai, K. Ando, K. Takanashi, S. Maekawa, and E. Saitoh, Nature (London) **464**, 262 (2010).
[5] H. Wu, L. Huang, C. Fang, B. S. Yang, C. H. Wan, G. Q. Yu, J. F. Feng, H. X. Wei, and X. F. Han, Phys. Rev. Lett. **120**, 097205 (2018).
[6] Y. Dai, S. J. Xu, S. W. Chen, X. L. Fan, D. Z. Yang, D. S. Xue, D. S. Song, J. Zhu, S. M. Zhou, and X. P. Qiu, Phys. Rev. B **100**, 064404 (2019).
[7] J. Xiao and G. E. W. Bauer, Phys. Rev. Lett. **108**, 217204 (2012).
[8] H. Nakayama, M. Althammer, Y. T. Chen, K. Uchida, Y. Kajiwara, D. Kikuchi, T. Ohtani, S. Geprags, M. Opel, S. Takahashi, R. Gross, G. E. W. Bauer, S. T. B. Goennenwein, and E. Saitoh, Phys. Rev. Lett. **110**, 206601 (2013).
[9] P. Li, T. Liu, H. Chang, A. Kalitsov, W. Zhang, G. Csaba, W. Li, D. Richardson, A. DeMann, G. Rimal, H. Dey, J. S. Jiang, W. Porod, S. B. Field, J. Tang, M. C. Marconi, A. Hoffmann, O. Mryasov, and M. Wu, Nat. Commun. **7**, 12688 (2016).

[10] C. O. Avci, A. Quindeau, C.-F. Pai, M. Mann, L. Caretta, A. S. Tang, M. C. Onbasli, C. A. Ross, and G. S. D. Beach, Nat. Mater. **16**, 309 (2017).

[11] A. Fert, N. Reyren, and V. Cros, Nat. Rev. Mater. **2**, 17031 (2017).

[12] A. Soumyanarayanan, N. Reyren, A. Fert, and C. Panagopoulos, Nature (London) **539**, 509 (2016).

[13] A. B. Butenko, A. A. Leonov, U. K. Rößler, and A. N. Bogdanov, Phys. Rev. B **82**, 052403 (2010).

[14] Y. Nii, T. Nakajima, A. Kikkawa, Y. Yamasaki, K. Ohishi, J. Suzuki, Y. Taguchi, T. Arima, Y. Tokura, and Y. Iwasa, Nat. Commun. **6**, 8539 (2015).

[15] K. K. Meng, J. Miao, X. G. Xu, Y. Wu, X. P. Zhao, J. H. Zhao, and Y. Jiang, Phys. Rev. B **94**, 214413 (2016).

[16] I. A. Ado, O. A. Tretiakov, and M. Titov, Phys. Rev. B **95**, 094401 (2017).

[17] Q. B. Liu, K. K. Meng, Y. Z. Cai, X. H. Qian, Y. C. Wu, S. Q. Zheng, and Y. Jiang, Appl. Phys. Lett. **112**, 022402 (2018).

[18] C. O. Avci, E. Rosenberg, L. Caretta, F. Büttner, M. Mann, C. Marcus, D. Bono, C. A. Ross, and G. S. D. Beach, Nat. Nanotechnol. **14**, 561 (2019).

[19] H. Wang, J. Chen, T. Liu, J. Zhang, K. Baumgaertl, C. Guo, Y. Li, C. Liu, P. Che, S. Tu, S. Liu, P. Gao, X. Han, D. Yu, M. Wu, D. Grundler, and H. Yu, Phys. Rev. Lett. **124**, 027203 (2020).

[20] J. Fu, M. Hua, X. Wen, M. Xue, S. Ding, M. Wang, P. Yu, S. Liu, J. Han, C. Wang, H. Du, Y. Yang, and J. Yang, Appl. Phys. Lett. **110**, 202403 (2017).

[21] L. Soumah, N. Beaulieu, L. Qassym, C. Carrétéro, E. Jacquet, R. Lebourgeois, J. B. Youssef, P. Bortolotti, V. Cros1, and A. Anane, Nat. Commun. **9**, 3355 (2018).

[22] C. T. Wang, X. F. Liang, Y. Zhang, X. Liang, Y. P. Zhu, J. Qin, Y. Gao, B. Peng, N. X. Sun, and L. Bi, Phys. Rev. B **96**, 224403 (2017).

[23] E. R. Rosenberg, L. Beran, C. O. Avci, C. Zeledon, B. Song, C. Gonzalez-Fuentes, J. Mendil, P. Gambardella, M. Veis, C. Garcia, G. S. D. Beach, and C. A. Ross, Phys. Rev. Mater. **2**, 094405 (2018).

[24] See Supplemental Material at http://link.aps.org/supplemental/10.1103/PhysRevB.101.174431 for more detailed discussion, which includes Refs. [25–32].

[25] A. Okada, S. Kanai, M. Yamanouchi, S. Ikeda, F. Matsukura, and H. Ohno, Appl. Phys. Lett. **105**, 052415 (2014).

[26] S. Iihama, Q. L. Ma, T. Kubota, S. Mizukami, Y. Ando, and T. Miyazaki, Appl. Phys. Express **5**, 083001 (2012).

[27] C. Hurd, *The Hall Effect in Metals and Alloys* (Plenum, New York, 1972).

[28] W. Y. Ching, Z. Gu, and Y. Xu, J. Appl. Phys. **89**, 6883 (2001).

[29] E. Liu, Y. Sun, N. Kumar, L. Muechler, A. Sun, L. Jiao, S. Yang, D. Liu, A. Liang, Q. Xu, J. Kroder, V. Süß, H. Borrmann, C. Shekhar, Z. Wang, C. Xi, W. Wang, W. Schnelle, S. Wirth, Y. Chen, S. T. B. Goennenwein, and C. Felser, Nat. Phys. **14**, 1125 (2018).

[30] B. F. Miao, S. Y. Huang, D. Qu, and C. L. Chien, Phys. Rev. Lett. **112**, 236601 (2014).

[31] K. K. Meng, X. P. Zhao, P. F. Liu, Q. Liu, Y. Wu, Z. P. Li, J. K. Chen, J. Miao, X. G. Xu, J. H. Zhao, and Y. Jiang. Phys. Rev. B **97**, 060407(R) (2018).

[32] N. Kanazawa, Y. Onose, T. Arima, D. Okuyama, K. Ohoyama, S. Wakimoto, K. Kakurai, S. Ishiwata, and Y. Tokura, Phys. Rev. Lett. **106**, 156603 (2011).

[33] J. F. K. Cooper, C. J. Kinane, S. Langridge, M. Ali, B. J. Hickey, T. Niizeki, K. Uchida, E. Saitoh, H. Ambaye, and A. Glavic, Phys. Rev. B **96**, 104404 (2017).

[34] S. M. Suturin, A. M. Korovin, V. E. Bursian, L. V. Lutsev, V. Bourobina, N. L. Yakovlev, M. Montecchi, L. Pasquali, V. Ukleev, A. Vorobiev, A. Devishvili, and N. S. Sokolov, Phys. Rev. Mater. **2**, 104404 (2018).

[35] Q. Shao, A. Grutter, Y. Liu, G. Yu, C. Y. Yang, D. A. Gilbert, E. Arenholz, P. Shafer, X. Che, C. Tang, M. Aldosary, A. Navabi, Q. L. He, B. J. Kirby, J. Shi, and K. L. Wang, Phys. Rev. B **99**, 104401 (2019).

[36] P. Hansen, P. Roschmann, and W. Tolksdorf, J. Appl. Phys. **45**, 2728 (1974).

[37] S. Vélez, A. Bedoya-Pinto, W. Yan, L. E. Hueso, and F. Casanova, Phys. Rev. B **94**, 174405 (2016).

[38] Y. T. Chen, S. Takahashi, H. Nakayama, M. Althammer, S. T. B. Goennenwein, E. Saitoh, and G. E. W. Bauer, Phys. Rev. B **87**, 144411 (2013).

[39] S. Meyer, R. Schlitz, S. Geprägs, M. Opel, H. Huebl, R. Gross, and S. T. B. Goennenwein, Appl. Phys. Lett. **106**, 132402 (2015).

[40] D. Liang, J. P. DeGrave, M. J. Stolt, Y. Tokura, and S. Jin, Nat. Commun. **6**, 8217 (2015).

[41] K. Shibata, X. Z. Yu, T. Hara, D. Morikawa, N. Kanazawa, K. Kimoto, S. Ishiwata, Y. Matsui, and Y. Tokura, Nat. Nanotech. **8**, 723 (2013).

[42] N. Vlietstra, J. Shan, V. Castel, B. J. van Wees, and J. Ben Youssef, Phys. Rev. B **87**, 184421 (2013).

[43] D. Xiao, M. C. Chang, and Q. Niu, Rev. Mod. Phys. **82**, 1959 (2010).

[44] A. Neubauer, C. Pfleiderer, B. Binz, A. Rosch, R. Ritz, P. G. Niklowitz, and P. Boni, Phys. Rev. Lett. **102**, 186602 (2009).

[45] M. Kimata, H. Chen, K. Kondou, S. Sugimoto, P. K. Muduli, M. Ikhlas, Y. Omori, T. Tomita, A. H. MacDonald, S. Nakatsuji, and Y. Otani, Nature (London) **565**, 627 (2019).

[46] Z. Hou, W. Ren, B. Ding, G. Xu, Y. Wang, B. Yang, Q. Zhang, Y. Zhang, E. Liu, F. Xu, W. Wang, G. Wu, X. Zhang, B. Shen, and Z. Zhang, Adv. Mater. **29**, 1701144 (2017).

[47] A. O. Leonov and M. Mostovoy, Nat. Commun. **6**, 8275 (2015).

[48] S. Nakatsuji, N. Kiyohara, and T. Higo, Nature (London) **527**, 212 (2015).

[49] A. Quindeau, C. O. Avci, W. Liu, C. Sun, M. Mann, A. S. Tang, M. C. Onbasli, D. Bono, P. M. Voyles, Y. Xu, J. Robinson, G. S. D. Beach, and C. A. Ross, Adv. Electron. Mater. **3**, 1600376 (2017).

[50] G. Singh, P. K. Rout, R. Porwal, and R. C. Budhani, Appl. Phys. Lett. **101**, 022411 (2012).

[51] G. N. Parker and W. M. Saslow, Phys. Rev. B **38**, 11718 (1988).

[52] A. Rosencweig, Can. J. Phys. **48**, 2857 (1970).

[53] B. A. AULD, Proc. IEEE **53**, 1517 (1965).

[54] A. Baena, L. Brey, and M. J. Calderón, Phys. Rev. B **83**, 064424 (2011).